

Computational Sports Aerodynamics of a Moving Sphere: Simulating a Ping Pong Ball in Free Flight

Kui Ou,* Patrice Castonguay,† and Antony Jameson ‡

Aeronautics and Astronautics Department, Stanford University, Stanford, CA 94305

Fluid dynamics associated with many sports involving spheric shaped equipments such as tennis, golf and ping pong balls tends to be very unsteady and viscous, with occasionally transitional behaviors. Some of the intricate aerodynamic behaviors are the mechanisms that make these sports competitive and spectacular. In this paper we discuss using high-order method as an effective method for solving unsteady fluid dynamics pertaining to sports. In particular, we perform direct numerical simulation of unsteady viscous flow past a spinning sphere. Taking a different approach from the usual computational practice of performing simulations of fixed free-stream and fixed Reynolds number flows, we compute the flow field around the spheric body together with the dynamic motion of the body. By coupling the sphere dynamic to the aerodynamic flow, we are able to simulate the flight trajectory of the sphere in free flight and examine the effect of introducing different varieties of spin on game play. The flow solver is based on the high-order Spectral Difference method. Coupling of fluid and structure is enforce weakly by advancing the equation of motion and flow equations in time together using the explicit multi-stage Runge-Kutta scheme. We rely on the inherent numerical dissipation in the high order method to resolve transitional flow, which effectively acts as a kind of implicit Large Eddy Simulation (ILES).

I. Introduction

While aeronautical applications are the major driving forces behind the development of computer and computational method for fluid flows, sports has also contributed to extending the capability of the computational fluid dynamics, albeit in a very different flow regime. The design of many sports equipments such as tennis ball, baseball, soccer ball, ping pong ball, golf ball and cricket ball is concerned with aerodynamics as much as the design of an aircraft wing . Aerodynamic design using computers to complement experimental approach is now a standard practice in industry. However it is sometimes surprising to realize what the computers can do, and cannot do. On the one hand, complex systems such as airplanes have been analyzed and designed using computers. On the other hand, a direct simulation of an unsteady viscous flow past a tennis ball is still a difficult problem. This is, of course, not a completely fair statement, because direct simulation of a airplane is far from tractable, even with the most powerful supercomputer available today. Fortunately airplanes are designed for stable steady cruise flight without complex unsteady aerodynamics. Hence the inviscid Euler equations sometimes can give fairly accurate prediction of the airplane performance very quickly. In this regard, steady high Reynolds number flow past an airfoil can be more manageable than unsteady low Reynolds number flow past a flying sports ball. Low Reynolds number flow past a small bluff body such as a sphere is highly unsteady and viscous. This is further complicated by the transitional behavior of the flow from laminar to turbulent in the transitional Reynolds number regime. The surface roughness of the sphere will determine the occurrence of the transition, significantly affecting the lift and drag exerted on the sphere, hence its trajectory. Popular sports, such as tennis, table tennis, baseball and soccer, all have very different surface textures. Some of them are specifically designed to exploit this transitional effect. The direct numerical simulation of low Reynolds number flow past a sphere remains very challenging. With the recent advance of computational algorithms and computation power, however, this problem is becoming

*PhD Candidate, Aeronautics and Astronautics Department, Stanford University, AIAA Student Member.

†PhD Candidate, Aeronautics and Astronautics Department, Stanford University, AIAA Student Member.

‡Thomas V Jones Professor, Aeronautics and Astronautics Department, Stanford University, AIAA Fellow.

tractable. While we used to be amused by the aerodynamic behaviors of various flying sports balls, the computers and computational methods have matured to a point when it is possible to understand the detailed aerodynamics of those sports balls in its fullness. In this paper, we investigate a spinning ping pong ball in free flight. Ping pong ball is chosen for its smooth surface and its small flight Reynolds number, compared to others. Generating geometries and creating meshes to resolve the fine surface details of tennis ball, baseball, or soccer ball are not simple tasks in themselves.

II. Problem Statement

Table tennis, or ping pong, is a popular sports. A ping pong ball has a weight, W , of 2.7g and a diameter, D , of 0.04m. Table tennis play is fast and demands quick reactions. The typical time it takes for a ping pong ball to fly across a table approaches the limit of human reaction time of about a quarter of a second. To take advantage of the opponent, a good player can introduce different varieties of spin to the ping pong ball, causing it to fly in different trajectories.

The ping pong ball is very light weight, and the sphere shape has a high drag coefficient. Therefore the aerodynamic forces and their influence on the ball's trajectory at low speeds are significant. The density of the air at sea level in the standard atmosphere is $\rho = 1.225 \text{ kg/m}^3$, the reference length is the diameter of the ball $D = 0.04$, and the viscosity of the air is $\mu = 1.789 \text{ e}^{-5}$. The Reynolds number of a ping pong ball as a function of ball flight velocity U is defined as

$$Re = \frac{\rho U L}{\mu} = 2739U$$

As an example of its flight speed, a ping pong ball in free fall in air will reach a terminal velocity of about 7 m/s in 0.6 s , traveling a distance of about 2 m . Hence a ping pong ball in free fall has a Reynolds number range of $Re = 0 - 19,000$. For the ping pong ball in table tennis play, in order to travel across the table length of 2.74 m within average human reaction time of 0.25 s , the average speed of the ping pong ball is $U_{ave} = 10 \text{ m/s}$. This will lead to an approximate average Reynolds number of $Re = 30,000$.

III. Numerical Method

For the fluid solver, we use the high order spectral difference method¹⁻⁵. The SD method, like Discontinuous Galerkin,⁶⁻¹¹ is element-wise discontinuous. Within each individual element, collocated solution and flux points are used to store flow solution and flow flux information. With these solution and flux points, one solution polynomial and one flux polynomial can be constructed to represent the flow solution and flux in the local domain spanned by the element. The flux polynomial is one order higher than the solution polynomial such that when it is differentiated the flux divergence is of the same order as the solution polynomial. Therefore, the number of flux points is one more than that of solution points. At the element interface, where two sets of local solution meet each other, the flux across the interface is discontinuous. A method to enforce continuity is to use a Riemann solver, which was developed to handle discontinuity across interface. Such a Riemann solver for enforcing flux continuity includes Roe¹³ flux or Rusanov¹⁴ flux. Details of the SD formulation are outlined in the subsequent section. The standard SD method, which follows the work by Sun etc,¹² is presented first. This is then followed by its extension to rotating/sliding boundary problem.

III.A. Spatial Discretization with Spectral Difference Method

Consider the unsteady compressible Navier-Stokes equations in conservative form written as:

$$\frac{\partial Q}{\partial t} + \frac{\partial F}{\partial x} + \frac{\partial G}{\partial y} + \frac{\partial H}{\partial z} = 0 \quad (1)$$

where $F = F_I - F_V$, $G = G_I - G_V$ and $H = H_I - H_V$. To achieve an efficient implementation, all element in the physical domain (x, y, z) are transformed into a standard cubic element, $0 \leq \xi \leq 1, 0 \leq \eta \leq 1, 0 \leq \zeta \leq 1$. The transformation can be written as

$$\begin{pmatrix} x \\ y \\ z \end{pmatrix} = \sum_{i=1}^K M_i(\xi, \eta, \zeta) \begin{pmatrix} x_i \\ y_i \\ z_i \end{pmatrix} \quad (2)$$

where K is the number of points used to define the physical elements, (x_i, y_i, z_i) are the Cartesian coordinates at those points, and $M_i(\xi, \eta, \zeta)$ are the shape functions. The metrics and Jacobian of the transformation can be computed for the standard element. The governing equations in the physical domain are then transferred into the computational domain, and the transformed equations take the following form:

$$\frac{\partial \tilde{Q}}{\partial t} + \frac{\partial \tilde{F}}{\partial \xi} + \frac{\partial \tilde{G}}{\partial \eta} + \frac{\partial \tilde{H}}{\partial \zeta} = 0 \quad (3)$$

where $\tilde{Q} = |J|Q$ and

$$\begin{pmatrix} \tilde{F} \\ \tilde{G} \\ \tilde{H} \end{pmatrix} = |J| \begin{pmatrix} \xi_x & \xi_y & \xi_z \\ \eta_x & \eta_y & \eta_z \\ \zeta_x & \zeta_y & \zeta_z \end{pmatrix} \begin{pmatrix} F \\ G \\ H \end{pmatrix} \quad (4)$$

The Jacobian matrix J is given by

$$J = \frac{\partial(x, y, z)}{\partial(\xi, \eta, \zeta)} = \begin{pmatrix} x_\xi & x_\eta & x_\zeta \\ y_\xi & y_\eta & y_\zeta \\ z_\xi & z_\eta & z_\zeta \end{pmatrix} \quad (5)$$

In the standard element, two sets of points are defined, namely the solution points and the flux points, as illustrated in Figure 1 for a 2D element. In order to construct a degree $(N-1)$ polynomial in each coordinate

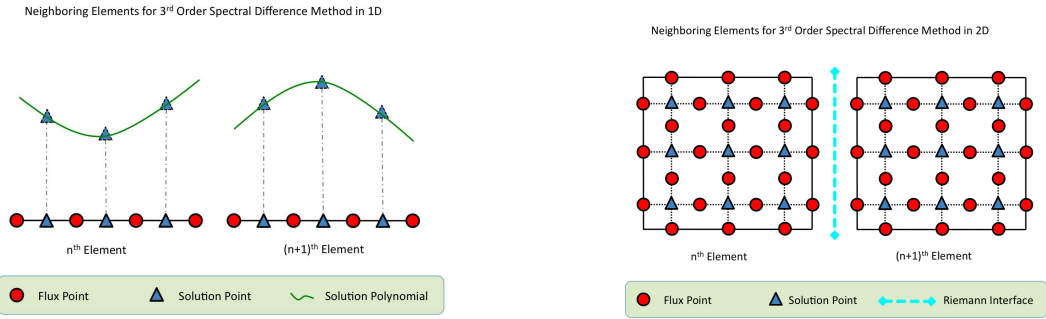


Figure 1: Position of solution (triangles) and flux (circles) points on the standard 1D (left) and 2D (right) element for 3rd order SD

direction, solution at N points are required. The solution points in 1D are chosen to be the Gauss points defined by:

$$X_s = \frac{1}{2} \left[1 - \cos \left(\frac{2s-1}{2N} \pi \right) \right], s = 1, 2, \dots, N. \quad (6)$$

The flux points were selected to be the Legendre-Gauss quadrature points plus the two end points 0 and 1, as suggested by Huynh.⁷ Choosing $P_{-1}(\xi) = 0$ and $P_0(\xi) = 1$, the higher-degree Legendre polynomials are

$$P_n(\xi) = \frac{2n-1}{n} (2\xi - 1) P_{n-1}(\xi) - \frac{n-1}{n} P_{n-2}(\xi) \quad (7)$$

The locations of these Legendre-Gauss quadrature points are the roots of equations $P_n(\xi) = 0$. They are generally found to be more stable than the Gauss-Lobatto flux points and produce more accurate solutions for high-order spectral difference schemes. Using the solutions at N solution points, a degree $(N-1)$ polynomial can be built using the following Lagrange basis defined as:

$$h_i(X) = \prod_{s=1, s \neq i}^N \left(\frac{X - X_s}{X_i - X_s} \right) \quad (8)$$

Similarly, using the fluxes at $(N + 1)$ flux points, a degree N polynomial can be built for the flux using a similar Lagrange basis as:

$$l_{i+1/2}(X) = \prod_{s=0, s \neq i}^N \left(\frac{X - X_{s+1/2}}{X_{i+1/2} - X_{s+1/2}} \right) \quad (9)$$

The reconstructed solution for the conserved variables in the standard element is the tensor product of the three one-dimensional polynomials,

$$Q(\xi, \eta, \zeta) = \sum_{k=1}^N \sum_{j=1}^N \sum_{i=1}^N \frac{\tilde{Q}_{i,j}}{|J_{i,j}|} h_i(\xi) h_j(\eta) h_k(\zeta) \quad (10)$$

Similarly, the reconstructed flux polynomials take the following form:

$$\begin{aligned} \tilde{F}(\xi, \eta, \zeta) &= \sum_{k=1}^N \sum_{j=1}^N \sum_{i=0}^N \tilde{F}_{i+1/2,j,k} \cdot l_{i+1/2}(\xi) \cdot h_j(\eta) \cdot h_k(\zeta) \\ \tilde{G}(\xi, \eta, \zeta) &= \sum_{k=1}^N \sum_{j=0}^N \sum_{i=1}^N \tilde{G}_{i,j+1/2,k} \cdot h_i(\xi) \cdot l_{j+1/2}(\eta) \cdot h_k(\zeta) \\ \tilde{H}(\xi, \eta, \zeta) &= \sum_{k=0}^N \sum_{j=1}^N \sum_{i=1}^N \tilde{H}_{i,j,k+1/2} \cdot h_i(\xi) \cdot h_j(\eta) \cdot l_{k+1/2}(\zeta) \end{aligned} \quad (11)$$

The reconstructed fluxes are only element-wise continuous, but discontinuous across cell interfaces. For the inviscid flux, a Riemann solver is employed to compute a common flux at interfaces to ensure conservation and stability. In our case, we have used both the Rusanov solver⁷ and the Roe solver to compute the interface inviscid fluxes. The viscous flux is a function of both the conserved variables and their gradients. Therefore, the solution gradients have to be calculated at the flux points. In our solver, the average approach described in reference⁷ is used to compute the viscous fluxes.

III.B. SD Extension to Rotating/Sliding Boundary Problem

The extension of the SD method to rotating boundary problem is straightforward by superimposing the rotating or sliding velocities on the boundary interface. Interesting results have been obtained for low Reynolds number laminar flow over a pair of rotating cylinders.¹⁷

III.C. Dynamic Trajectory Calculation

In this study, we consider the interaction between a sphere and its external flow. For the structure model of the sphere, we use a simple finite mass model to represent the dynamic of the sphere. The sphere is free to move in the three-dimensional space. The sphere movement and trajectory is driven by the force exerted by the external fluid flow and the gravitational force. The governing equation for the simplified structure model is expressed as follows:

$$M\mathbf{a} = \mathbf{F} \quad (12)$$

where M is the mass of the sphere, \mathbf{F} is the external force, which is equal to the lift exerted on the sphere due to the fluid flow and \mathbf{a} is the acceleration of the sphere. The second order dynamic equation can be written as a system of first order differential equations as follows:

$$M\dot{\mathbf{v}} = \mathbf{F} \quad (13)$$

$$\dot{\mathbf{x}} - \mathbf{v} = 0 \quad (14)$$

where \mathbf{v} is the velocity vector, and \mathbf{x} is the position coordinates of the sphere. The system of first order equations can then be solved with the fourth order Runge-Kutta method, which is the same time integrator used in the fluid solver.

III.D. Dynamic Coupling

The coupling of the sphere dynamics and fluid equations is enforced at each Runge-Kutta stage. For this reason, a five-stage Runge-Kutta method is used. At each RK stage, the lift force from the fluid solver is passed to the sphere; the sphere dynamic is then calculated; and the kinematic information, i.e. the displacement and velocity, is passed back to the fluid solver which then advances to the next RK stage; the whole process is then repeated.

IV. Numerical Results Part I - 2D Simulation

IV.A. Previous Study of Fluid Structure Interaction

The fluid-structure interaction methodology outlined in the previous sections has been implemented and applied to various applications. In these studies, it has been demonstrated that the current method works well for simple structure models such as the spring-mass-damper model for modeling an elastic cylinder, and the Bernoulli-Euler beam model for representing an elastic beam. References to these work can be found here.^{18, 19}

IV.B. Free-Falling Cylinder

In the previous referenced studies, the fluid-structure interaction framework was developed for a fixed uniform flow. A ping pong ball in flight is also subject to gravitational force. Gravity, together with the time (and speed) dependent drag force, will cause the ping pong ball to decelerate along its path. In this section, we simulate this scenario by considering a model problem with a free-falling cylinder. For the flow conditions, we choose the non-dimensional speed of sound to be 1, the viscosity to be $4e-8$, the non-dimensional gravitational force to be 0.02885, the mass of the cylinder to be 0.0027, and the cylinder diameter to be 0.04. Since the velocity of the cylinder will change dynamically during the free-fall, the Mach number and Reynolds number also change dynamically. The results are presented in Figure (2), where the time histories of the drag, velocity and distance travelled during the free fall are plotted. The cylinder reaches a terminal velocity when aerodynamic force and gravitational force are in balance - a result that we expect from experience and intuition. Figure (3)(a) plots the various positions of the cylinder in its path during the free fall. Each

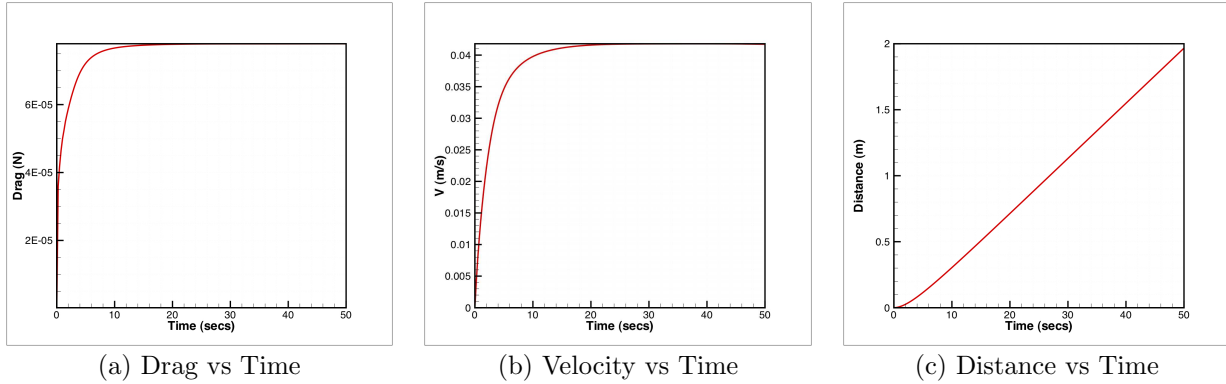
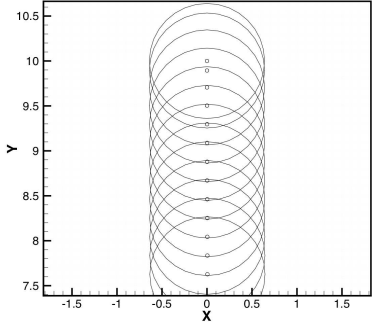


Figure 2: The time evolution of drag, velocity and distance of a free falling cylinder

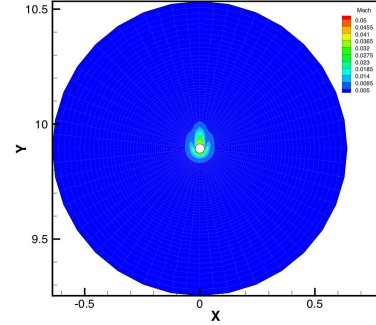
frame is taken at constant time interval. The resulting terminal velocity is evident from the constant spacing between each frame at the later stage of the trajectory. The Mach contours are plotted in Figure (3)(b) to (d) for different time instances. The 2D simulation of the free-falling cylinder provides encouraging results that allow us to move onto 3D simulation of a free-flying sphere under a dynamic environment.

IV.C. Flight Trajectory of a Cylinder

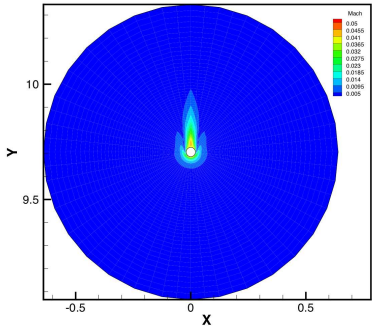
Having so far considered a couple of two-dimensional applications as building blocks for our eventual objective of simulating a spinning ping pong ball in free-flight, we perform a few tests to demonstrate the capability we have so far developed. Although the following examples are still two-dimensional, the extension to three-dimensional application is straightforward. In the following sections, we simulate the free flights of a



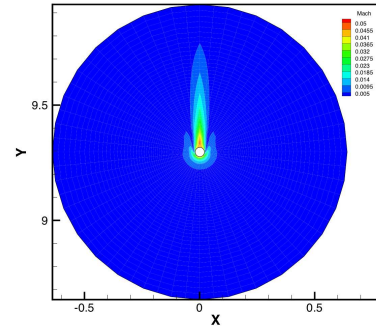
(a) Free Fall Path



(c) Mach contour shortly after release



(e) Mach contour during acceleration



(f) Mach contour near terminal velocity

Figure 3: Mach contours of a free falling cylinder

2D cylinder with and without spinning, and illustrate the effect of various spinning directions on flight trajectories. In all cases, the non-dimensional speed of sound is 1 and the viscosity is 0.001. At the starting point, the cylinder is given an initial speed of 0.2 in the x-direction and 0.2 in the y-direction. The non-dimensional mass of the cylinder is 5. The non-dimensional gravitational acceleration is 0.0002. The computational mesh, at its coarsest level, is shown in Figure (4)(a).

IV.C.1. Flight Trajectory of a Cylinder in Projectile Motion with and without Spin

In the first case, we consider the flight of the cylinder with zero rotational speed. The snapshots of the cylinder are recorded at equal time interval and plotted in Figure (4)(b). This acts as a reference flight path to evaluate the effect of spinning, which is considered next.

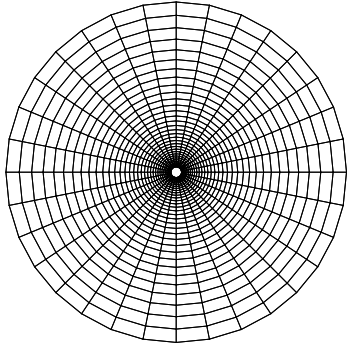
In the second case, the cylinder is given a clockwise non-dimensional rotational speed of $\Omega = 0.05$. The down force acting on the cylinder due to the forward spin results in a trajectory that is lower in height and shorter in distance, as illustrated in Figure (4)(c).

In the third case, the cylinder is given an anti-clockwise non-dimensional rotational speed of $\Omega = 0.02$. The lifting force acting on the cylinder due to the under-spin allows the cylinder to reach a higher altitude, travel a longer distance, and impact the floor with a shallower angle, as shown in Figure (4)(d).

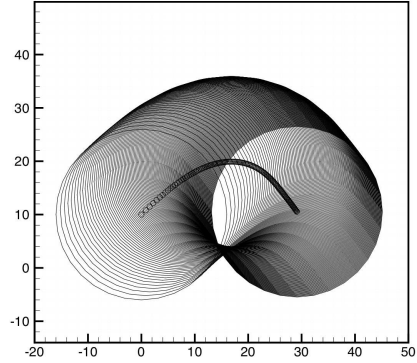
V. Numerical Results Part II - 3D Validation

V.A. Flow over a Stationary Sphere

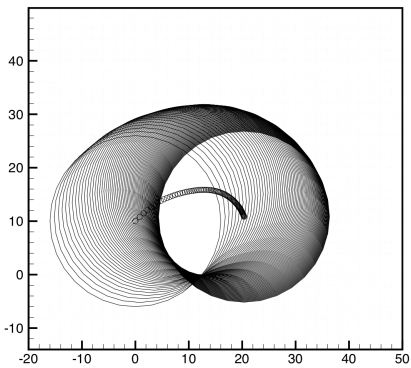
3D simulations of flow over a stationary sphere have been performed. Unstructured hexahedral mesh elements were generated in a rectangular flow domain using the GridPro grid generator. The outline of the flow domain is plotted in Figure (5)(b), together with a representative example of flow domain partitioning. There is a total of 173,942 elements in the starting mesh. The 4th order SD3D method is used. Zoom of the mesh



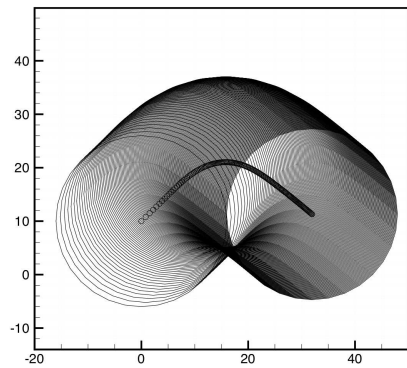
(a) computational mesh



(b) moving cylinder without spin



(c) moving cylinder with clockwise rotation



(d) moving cylinder with anti-clockwise rotation

Figure 4: Flight paths of a cylinder in projectile motion with an initial speed of 0.2 in the x-direction and 0.2 in the y-direction.

at its center plane is shown in Figure (7)(b), showing all the degrees of freedom for the second order case. The surface mesh of the sphere is shown in Figure (9)(b). The flow conditions are Mach=0.1 and Re=300. This follows from previous studies of laminar flow over a sphere under the same flow conditions.²⁰⁻²³ The comparison of results with previous computational results and experimental measurements is summarized in Table 1. The present calculation is in great agreement with the previous simulations as well as the experimental measurement. In our study, we observe that a steady state solution can also be obtained.

Data Set	Time Averaged Lift Coefficient \bar{C}_L	Time Averaged Drag Coefficient \bar{C}_D
Computed by ²¹	0.069	0.656
Computed by ²⁰	0.067	0.658
Computed by ²³	0.065	0.655
Measured by ²²	-	0.629
Present SD3D (unsteady)	0.064	0.654
Present SD3D (steady)	0	0.652

Table 1: Measured and computed time-averaged lift and drag coefficients of the flow over a sphere at $Re = 300$ and $Mach = 0.1$.

V.A.1. Steady Solution

The steady state results are shown in Figure(5). In Figure(5)(a) the streamlines past the sphere are plotted. In Figure (5) (c) and (d) the pressure and Mach contours in the x-y plane are plotted. The flow solution is symmetric and there is no periodic vortex-shedding. The temporal variations of the lift and drag coefficients

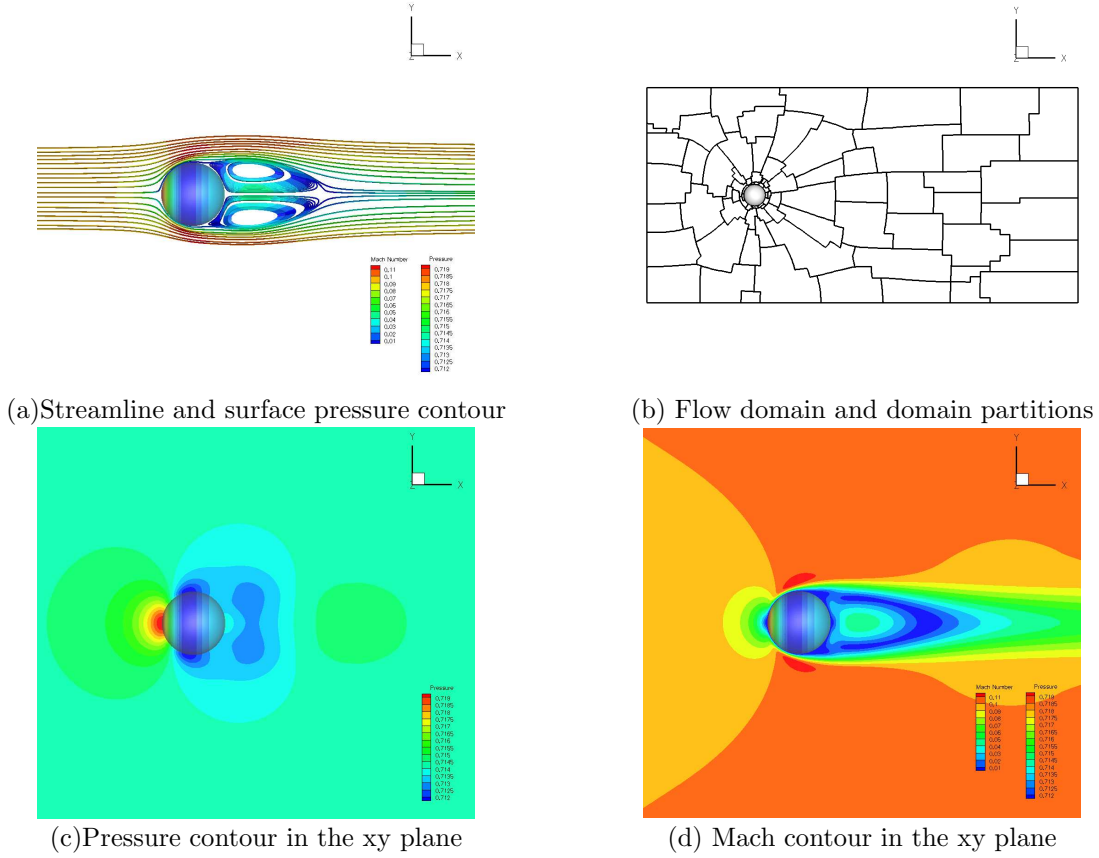


Figure 5: Results for flow over a stationary sphere at Mach=0.1 and Re=300

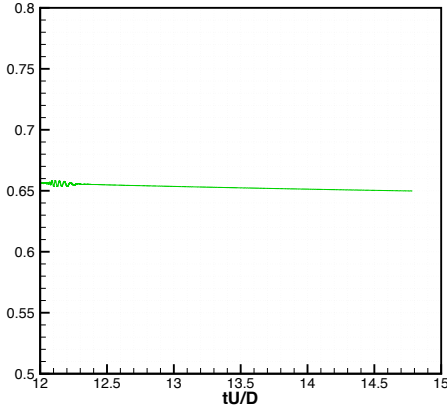
are plotted in Figure (6)(a) and (b). The steady nature of this solution is apparent from the lack of the frequency contents in the lift and drag variations.

V.A.2. Unsteady Solution

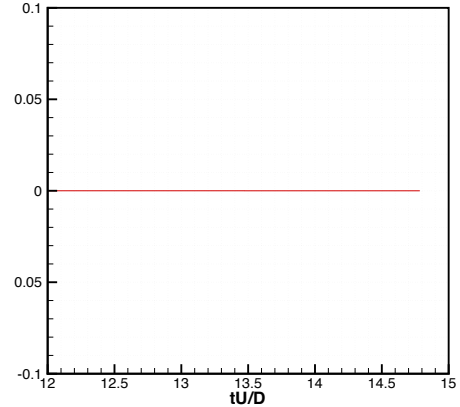
The unsteady solution of the flow past a stationary sphere can be obtained by initially perturbing the flow and then allowing the simulation to converge to periodic steady state after the perturbation is removed. The streamline pattern, pressure and Mach contours of the resultant unsteady flow are plotted in Figure (7). From the plots, we see that shedding solutions were obtained. The temporal variations of the lift and drag coefficients are plotted in Figure (8)(a) and (b).

V.B. Flow over a Spinning Sphere

Simulation of flow over a spinning sphere was investigated and the results are presented in this section. The same mesh and flow conditions as before were used. Laminar flow over a spinning sphere at $Re=300$ was previously studied by Kim in the referenced study.²⁰ In this section we compare our present results with the results by Kim, both quantitatively, in terms of streamline pattern, and qualitatively, in terms of aerodynamic force coefficients. The non-dimensional rotational speed is defined as $\Omega = \frac{\omega R}{U_\infty}$. We consider the case of $\Omega = 0.6$, with the axis of rotation being in the transverse direction, i.e. perpendicular to the streamwise flow. The resulting flow with $\Omega = 0.6$ reaches a steady state. The streamline pattern is plotted in Figure(9)(a). The downward deflection of the streamline is easily observed. In the x-y plane that cuts through the center of the sphere, we plot the pressure and mach contours together with the streamline

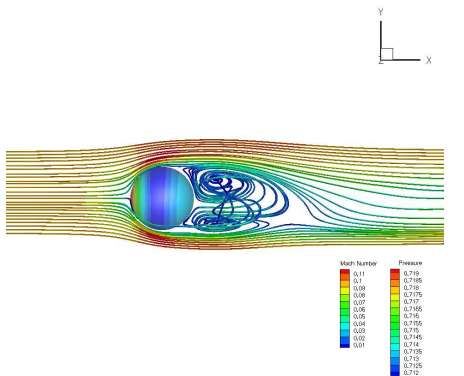


(a) CL vs Time

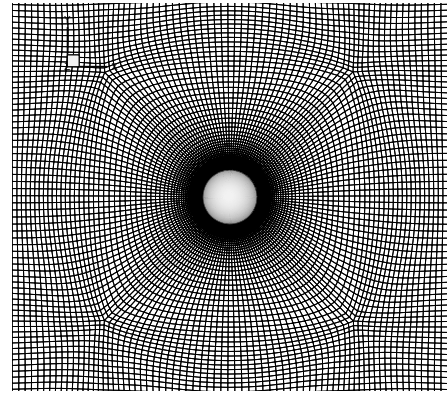


(b) CD vs Time

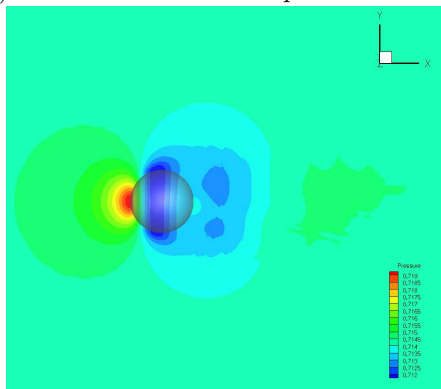
Figure 6: Temporal variations of the lift and drag coefficients for the steady-state solution of the flow past a stationary sphere



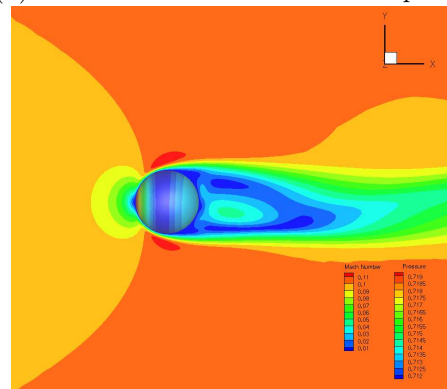
(a) Streamline and surface pressure contour



(b) Zoom of the mesh around the sphere



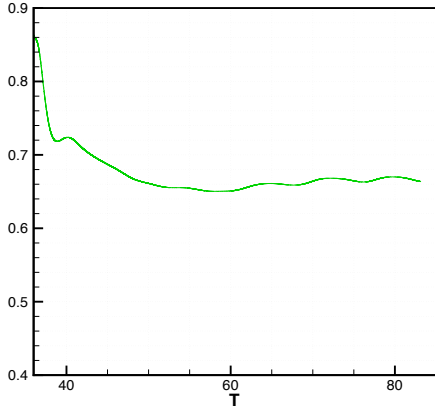
(c) Pressure contour in the xy plane



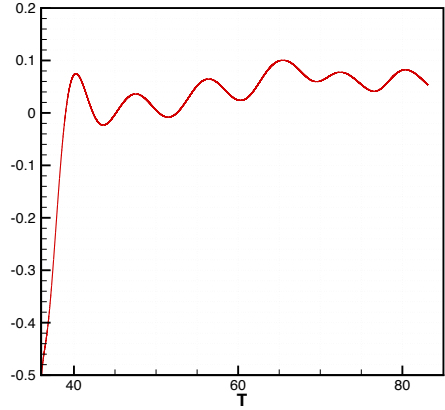
(d) Mach contour in the xy plane

Figure 7: Results for unsteady flow over a stationary sphere at Mach=0.1 and Re=300

pattern in Figure(9)(c) and (d). In this plane the effect of spinning can be more clearly observed. The rotation of the sphere in the anti-clockwise direction leads to high local speed. This results in a low pressure region underneath the sphere, where the direction of sphere rotation is in line with the freestream flow. This results in lift being generated perpendicular to the freestream flow. The streamline pattern of the present result is compared with the one obtained by Kim. The quantitative agreement of the flow pattern is very

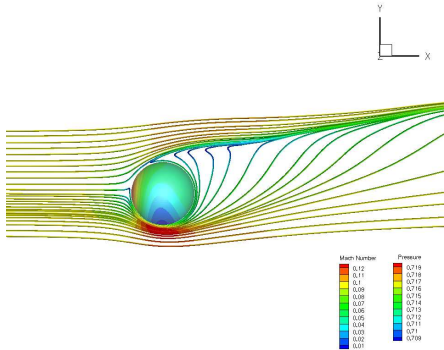


(a) CL vs Time

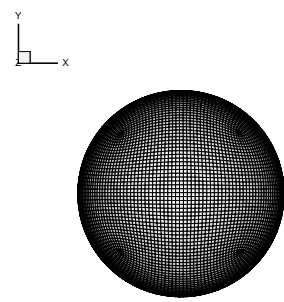


(b) CD vs Time

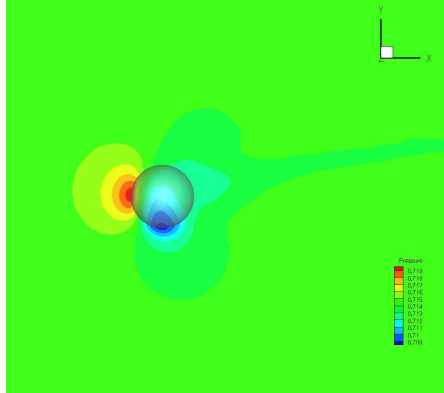
Figure 8: Temporal variations of the lift and drag coefficients for the unsteady solution of the flow past a stationary sphere



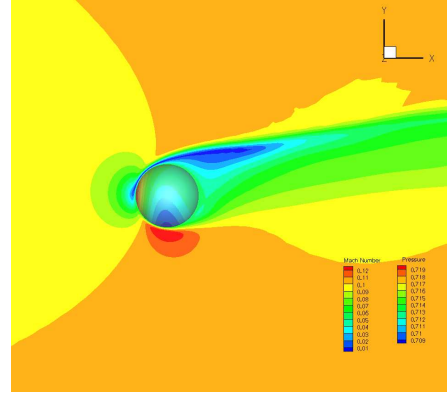
(a) Streamline and surface pressure contour



(b) Sphere surface mesh



(c) Pressure contour in the xy plane



(d) Mach contour in the xy plane

Figure 9: Results for flow over a spinning sphere at Mach=0.1 and Re=300. The sphere is rotating with a non-dimensionalized rotational speed of $\Omega = 0.6$

good, as shown in Figure(10)(a) and (d). The predictions of the aerodynamic lift and drag coefficients are also in good agreements with Kim's work. The comparison is summarized in Table (2).

Data Set	Time Averaged Lift Coefficient \bar{C}_L	Time Averaged Drag Coefficient \bar{C}_D
Computed by ²⁰	0.50	0.84
Present SD3D	0.52	0.857

Table 2: Computed time-averaged lift and drag coefficients of the flow over a spinning sphere at $Re = 300$, $Mach = 0.1$ and $\Omega = 0.6$.

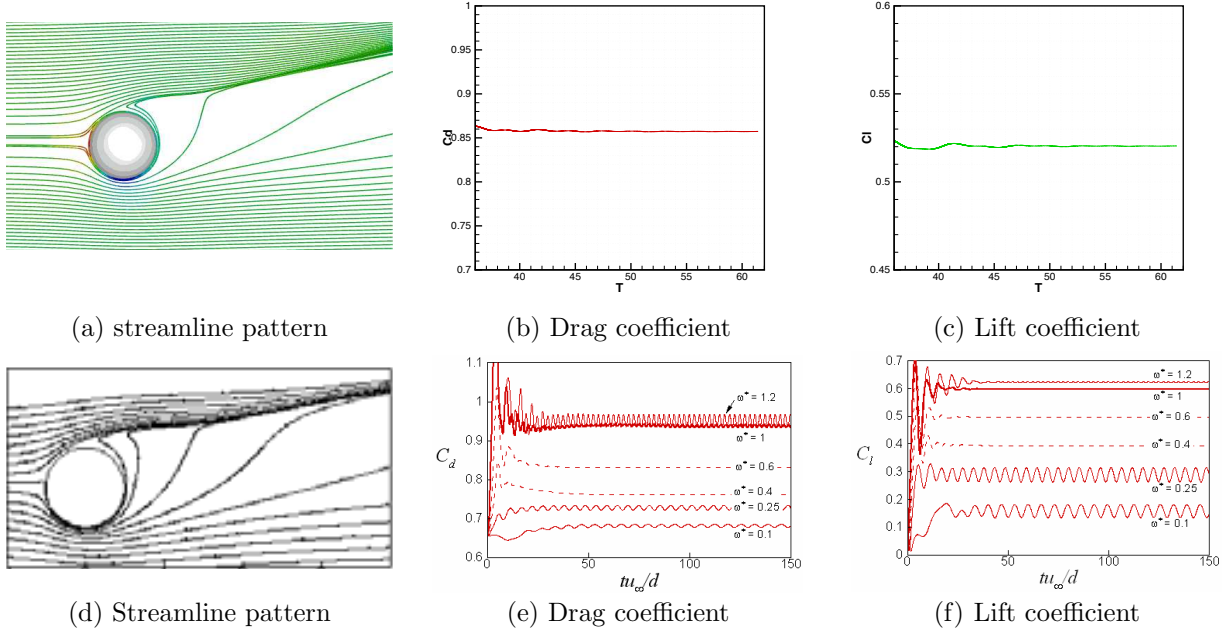


Figure 10: Comparison of the flow streamline pattern and the aerodynamic lift and drag coefficients between the present study (top row) and the study by Kim²⁰ (bottom row) at $Mach=0.1$ and $Re=300$, for the sphere rotating with a non-dimensionalized rotational speed of $\Omega = 0.6$

VI. Numerical Results Part III - Simulation of A Flying Ping Pong Ball

In the previous two sections, the numerical framework for fluid structure interaction in a dynamic environment was first developed and demonstrated for 2D applications. Subsequently, 3D validations were carried out for flows over a sphere. In the current section, simulation results of a ping pong ball under projectile motion are discussed. The flight trajectory of the ping pong ball was traced. The effects of rotation were also studied by comparing the resultant trajectories, aerodynamic forces, and the details of the flow fields for the ping pong ball spinning along different axes.

The computational mesh is similar to the mesh used in the previous section. However, instead of a rectangular box, a spherical flow domain is constructed. The farfield boundary is 20 chord away from the sphere surface. The mesh consists of a total of 321,408 elements. The flow conditions are as follows: pressure $p = 1.01325E^4$, density $\rho = 1.225$, viscosity $\mu = 1.789E^{-5}$, ping pong ball diameter $d = 0.04$, ping pong ball mass $m = 0.0027$, gravitational force $g = 9.81$. Except for pressure, the above values are chosen to be as close to real flow conditions a ping pong ball is subjected to as possible. The pressure is chosen to be slightly smaller so that the resultant Mach number is not too restrictively small for the present compressible flow solver. The ping pong ball is given an initial speed and initial angle of projection. The following values are used: projectile angle $\alpha_0 = 10^\circ$, x-direction speed $u_x = 9.8481$, and y-direction speed $u_y = 1.7365$. The initial velocity of $v = 10m/s$ corresponds to $Re = 27,390$ and $Mach = 0.1$. Fourth order SD solutions were computed.

VI.A. Flight Trajectory of A Non-spinning Ping Pong Ball

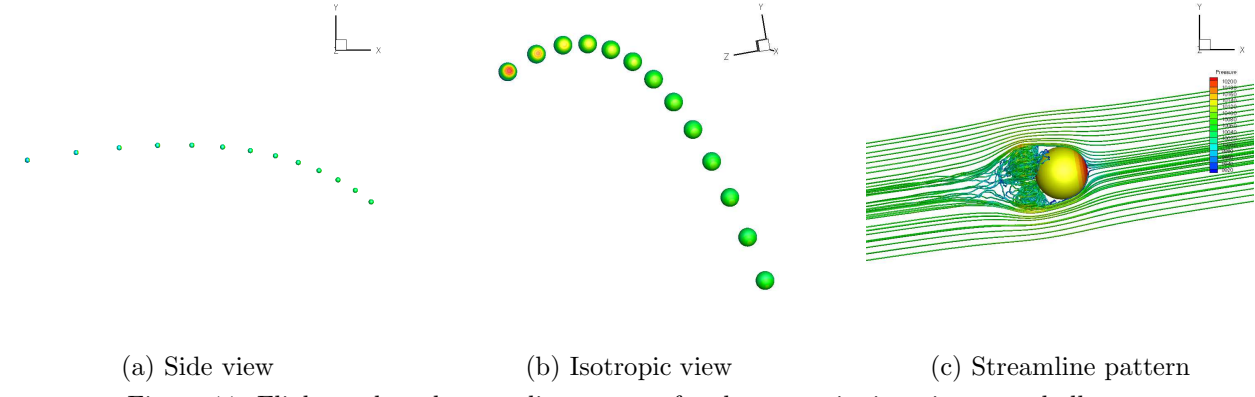


Figure 11: Flight path and streamline pattern for the non-spinning ping pong ball

In the first simulation, we consider the case of a non-spinning ping pong ball. For this case, we have, for the non-dimensional rotation speed, $\Omega = 0$. The flight path for the non-spinning case is recorded by taking snapshots of the ping pong ball at an equal time interval of $\Delta t = 0.4\text{sec}$. This is plotted in Figure 11 (a) and (b) in the x-y plane view and in isotropic view respectively. The surface contour indicates the pressure level. To visualize the flow fields around the ping pong ball, the streamline pattern at its initial position is plotted in Figure 11 (c).

VI.B. Effect of Spinning Part I - Top Spin

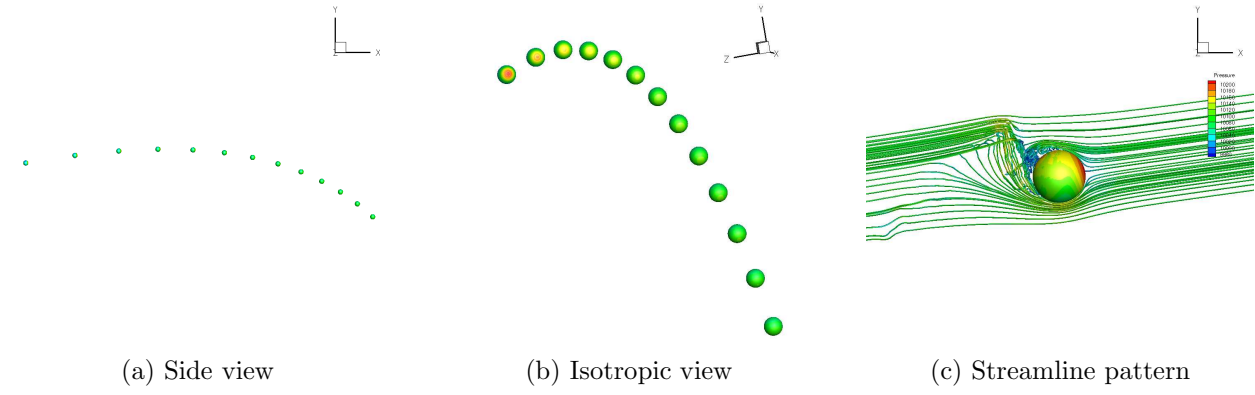


Figure 12: Flight path and streamline pattern for the top-spinning ping pong ball

In the second simulation, we consider the case of the ping pong ball with a clockwise rotation along the z-axis. We refer to this as top-spin. For this case, the non-dimensional rotation speed is $\Omega = 0.5$. The resultant flight path is plotted in Figure 12 (a) and (b) in the x-y plane view and in isotropic view respectively. The streamline pattern at its initial position is plotted in Figure 12 (c). The effect of clockwise rotation on the flow fields can be readily observed from the upward deflections of the streamlines in the wake of the ping pong ball. Correspondingly, a relatively low pressure region is developed near the lower side of the sphere. These evidences suggest that by introducing top spin to the ping pong ball, a downward force is produced. To investigate the effect of the downward force on the ping pong ball flight trajectory, we can examine Figure 11 more carefully. Comparing Figure 11 (b) with Figure 12 (b), we note that, firstly, the final position of the top-spinning ping pong ball is lower than the non-spinning case, indicating that a top-spun ping pong ball will hit the table earlier. Secondly, the peak of the top-spinning trajectory is shifted leftwards, compared to the non-spinning case. Lastly, the angle of entry is steeper for the top-spinning case than for the non-spinning case.

VI.C. Effect of Spinning Part II - Under Spin

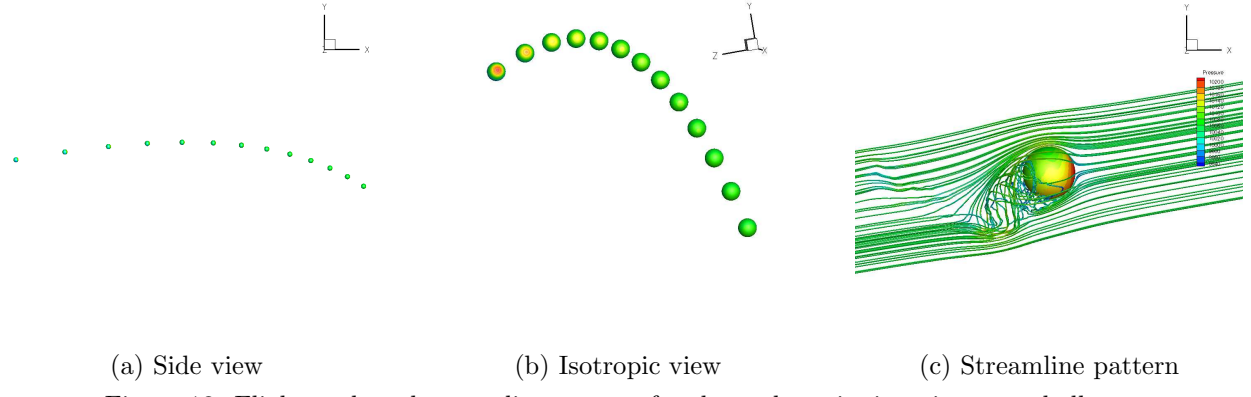


Figure 13: Flight path and streamline pattern for the under-spinning ping pong ball

In the third simulation, we consider the case of the ping pong ball with an anti-clockwise rotation along the z-axis. We refer to this as under-spin. For this case, the non-dimensional rotation speed is $\Omega = -0.5$. The resultant flight path is plotted in Figure 13 (a) and (b) in the x-y plane view and in isotropic view respectively. The streamline pattern at its initial position is plotted in Figure 13 (c). Compare to the previous top-spinning case, the reversal of the spinning direction has an opposite effect on the flow fields and resultant flight path. Flows were deflected downwards and a low pressure region was created on the upper surface of the sphere. The upward lift allows the ping pong ball to fly further with a shallower profile.

VI.D. Effect of Spinning Part III - Side Spin

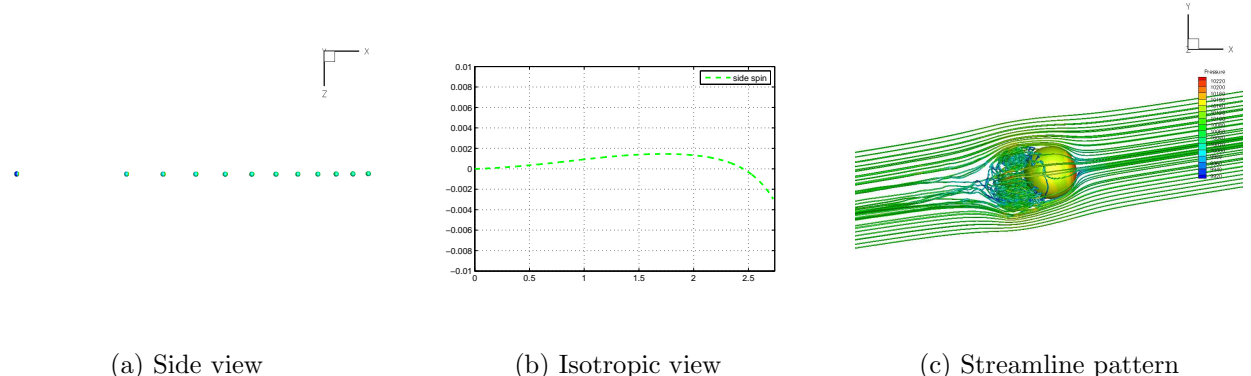


Figure 14: Flight path and streamline pattern for the side-spinning ping pong ball

In the last simulation, we consider the case of the ping pong ball with a rotation along the streamwise x-axis. We refer to this as side-spin. For this case, the non-dimensional rotation speed is $\Omega = 0.5$. The streamline pattern at its initial position is plotted in Figure 14 (c). The resultant flight path in the x-y plane is very similar to the non-spinning case, indicating that the effects of spinning along different axes are not closely coupled. The resultant flight path in the x-z plane is plotted in Figure 14 (a). Examining the flight path carefully, we observe that side-spin leads to an S-shape trajectory when viewing from the top. In another word, the ping pong ball first curved to the left and then right as it flew across the table. This is more clearly illustrated in Figure 14 (b). This occurred because the vertical velocity changed directions as the ping pong ball rose and fell. The effect of side-spinning along the streamwise axis (i.e. x-axis) is to induce leftward force during the rise and a rightward force during the fall.

VI.E. Details of the Flow Fields and Comparison of Flight Paths

The flow fields around the ping pong ball under different spinning scenarios are plotted in Figure 15.

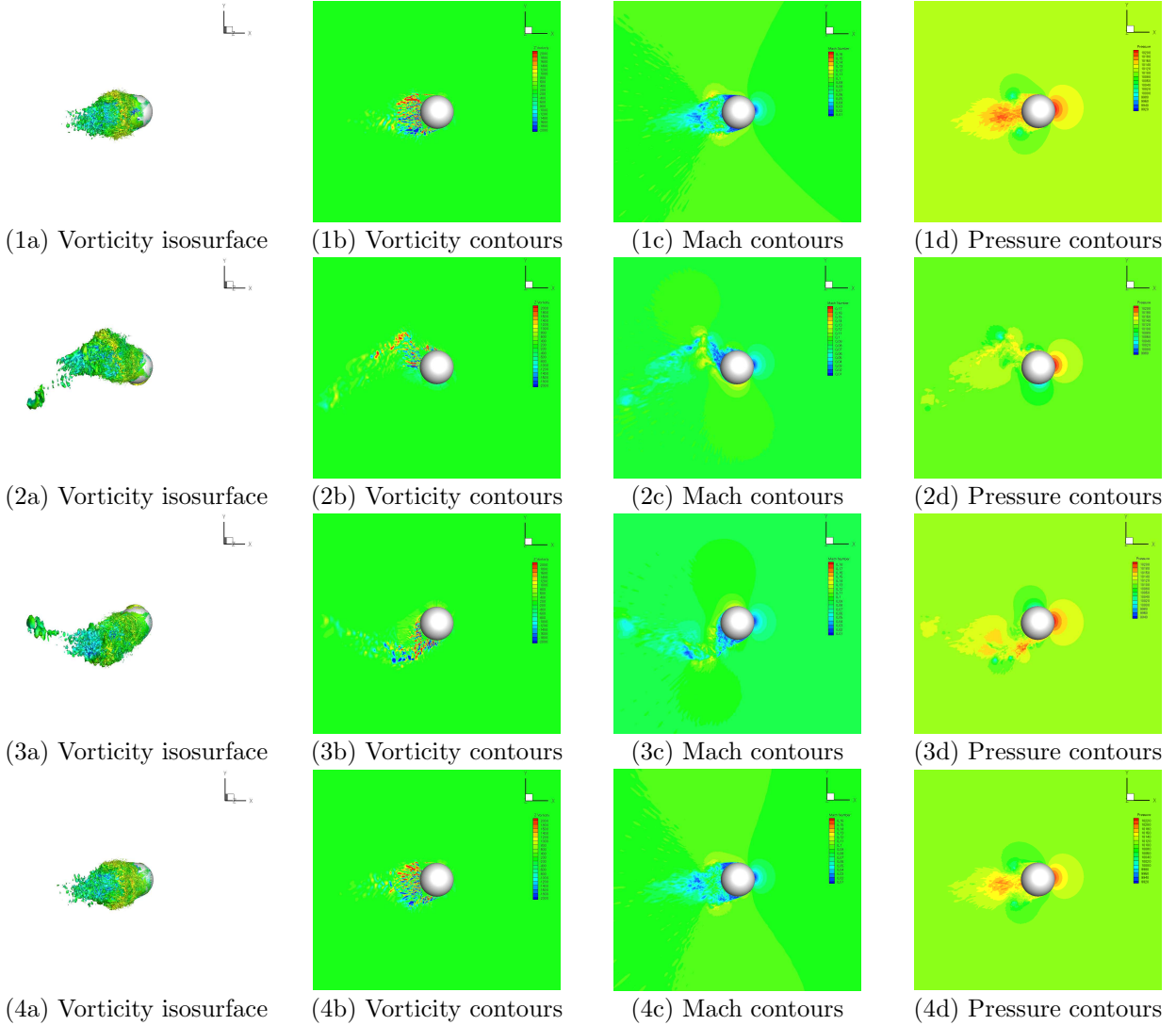


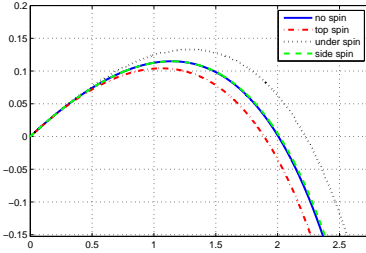
Figure 15: Instantaneous flow fields near the sphere. Solutions for the non-spinning case are plotted in the first row. Solutions for the top-spinning case are plotted in the second row. Solutions for the under-spinning case are plotted in the third row. Solutions for the side-spinning case are plotted in the fourth row.

The resultant flight paths of the ping pong ball under different spinning scenarios, as discussed in the earlier sections, are summarized in Figure 16 (a) and (c). The distinctions between all four cases are clearly illustrated in these plots. In summary, the top spin ball has a stronger arc in its trajectory. The under spin ball has a relatively flatter trajectory. The effect of increasing the rotational speed has also been investigated. Two additional cases were computed and the results are plotted in Figure 16 (b) and (d). These cases further support the previous findings.

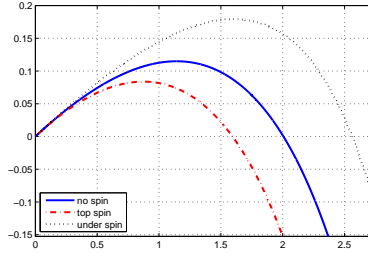
The x-axis range of the plots corresponds to the length of a standard table tennis table, which is 2.74m. Also, for reference, the table tennis net has a height of 0.1525m. The simulations have been setup assuming that the ping pong ball is struck at the edge of the table and at a height equal to the top position of the net. From the plots, it can be seen that the ping pong ball under nearly all the spinning scenarios considered here is able to clear the net and hit the table.

VII. Conclusion

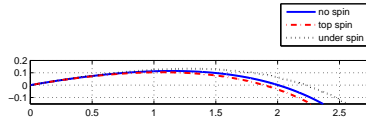
In this paper, we investigated unsteady fluid dynamics of flow over a spinning smooth sphere using high order SD method. Numerical tests have been performed to validate the solver for spinning and non-spinning



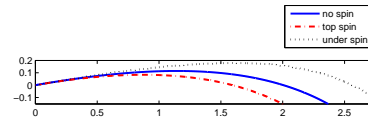
(a) Zoom of the flight trajectories for $\Omega = 0.5$



(b) Zoom of the flight trajectories for $\Omega = 1.0$



(c) flight trajectories for $\Omega = 0.5$



(d) flight trajectories for $\Omega = 1.0$

Figure 16: Summary of the flight trajectories for a ping pong ball under different spinning scenarios.

spheres at laminar Reynolds number. The present results are in very good agreement with the existing work in the literature. In addition, a numerical framework has been setup to couple the flow equations with the equation of motion of a rigid body. This makes it possible to compute the unsteady aerodynamic of a spinning and moving sphere under a very dynamic environment. The flow solver was applied to simulate a real ping pong ball in flight. Several simulations were performed with the ping pong ball spinning along different axes, with different magnitudes. The resultant flight trajectories of these simulated cases reveal the effect of different varieties of spin on the ping pong ball. It is found that the top spin ping pong ball has a stronger arc in its trajectory. The under spin ping pong ball has a relatively flatter trajectory. Spinning the ping pong ball along the streamwise axis leads to a wobbling path in such a way that, during the flight the ping pong ball curves to one side as it rises and curves to the other side as it falls. Finally the flow fields around the ping pong ball exhibits transitional behaviors. Many small scaled turbulent like flow structures were observed from the simulation results. These flow features were resolved by the present flow solver without any subgrid scaled model. The inherent numerical dissipation in the high order method could potentially act as a kind of implicit Large Eddy Simulation, though further investigations are needed to better support this.

VIII. Acknowledgements

This research has been made possible through the support of the Air Force Office of Scientific Research under grants FA9550-07-1-095 and FA9550-10-1-0418, and the National Science Foundation under grants 0708071 and 0915006. The authors would also like to thank Peter Eiseman of Program Development Company for providing the GridPro meshing software that is used for creating and gridding the sphere.

References

- ¹D. A. Kopriva and J. H. Kolias, *A conservative staggered-grid Chebyshev multidomain method for compressible flows*, *J. Comput. Phys.* **125**, 244 (1996).
- ²Y. Liu, M. Vinokur, and Z. J. Wang, *Spectral difference method for unstructured grids I: basic formulation*, *J. Comput. Phys.* **216**, 780 (2006).
- ³Z. J. Wang, Y. Liu, G. May, and A. Jameson, *Spectral difference method for unstructured grids II: extension to the Euler equations*, *J. Sci. Comput.* **32**, 45 (2007).
- ⁴C. Liang, S. Premasuthan, and A. Jameson, *High-order accurate simulation of low-Mach laminar flow past two side-by-side cylinders using spectral difference method*, *Comput. Struct.* **87**, 812 (2009).

- ⁵C. Liang, A. Jameson, and Z. J. Wang, *Spectral difference method for compressible flow on unstructured grids with mixed elements*, J. Comput. Phys. **228**, 2847 (2009).
- ⁶W. H. Reed and T. R. Hill, *Triangular mesh methods for the neutron transport equation*, Technical Report LA-UR-73-479, Los Alamos National Laboratory, Los Alamos, New Mexico, USA, 1973.
- ⁷B. Cockburn and C. Shu, *Runge-Kutta Discontinuous Galerkin Methods for Convection-Dominated Problems*, J. Sci. Comput. **16**, 173 (2001).
- ⁸D. N. Arnold, F. Brezzi, B. Cockburn, and L. D. Marini, *Unified analysis of discontinuous Galerkin methods for elliptic problems*, SIAM J. Numer. Anal. **39**, 1749 (2001).
- ⁹J. S. Hesthaven and T. Warburton, *Nodal discontinuous Galerkin methods - Algorithms, analysis, and applications*, Springer, (2008).
- ¹⁰J. S. Hesthaven and T. Warburton, *Nodal high-order methods on unstructured grids*, J. Comput. Phys. **181**, 186 (2002).
- ¹¹F. X. Giraldo, J. S. Hesthaven, and T. Warburton, *Nodal high-order discontinuous Galerkin methods for the spherical shallow water equations*, J. Comput. Phys. **181**, 499 (2002).
- ¹²Y. Sun, Z. J. Wang, and Y. Liu *High-Order Multidomain Spectral Difference Method for the Navier-Stokes Equations on Unstructured Hexahedral Grids*, Communications in Computational Physics **Vol 2**, Number 2, pp 310-333 (2006).
- ¹³P. L. Roe, *Approximate Riemann solvers, parameter vectors, and difference schemes*, J. Comput. Phys. **43**, 357 (1981).
- ¹⁴V. V. Rusanov, *Calculation of interaction of non-steady shock waves with obstacles*, Journal of Computational Math Physics USSR, Vol. 1, pp.261-279, 1961.
- ¹⁵H. T. Huynh, *A flux reconstruction approach to high-order schemes including discontinuous Galerkin methods*, Number AIAA-2007-4079, AIAA Computational Fluid Dynamics Conference, 2007.
- ¹⁶A. Jameson, *A proof of the stability of the spectral difference method for all orders of accuracy*, J. Sci. Comput. (2010).
- ¹⁷K. Ou, C. Liang, S. Premasuthan, and A. Jameson, *High-Order Spectral Difference Simulation of Laminar Compressible Flow Over Two Counter-Rotating Cylinders*, AIAA-2009-3956, 27th AIAA AA Conference, San Antonio, June 2009.
- ¹⁸K. Ou and A. Jameson *A High- Order Spectral Difference Method for Fluid- Structure Interaction on Dynamic Deforming Meshes*, AIAA-2010-4932, 28th AIAA Applied Aerodynamics Conference, Chicago, Illinois, 28 Jun - 1 Jul 2010
- ¹⁹K. Ou and A. Jameson *Flow Induced Cylinder Oscillation and Its Control with High Order Spectral Difference Method on Deformable Mesh*, ASME 2010 3rd Joint US-European Fluids Engineering Summer Meeting, Montreal, Quebec, Canada, 1 August - 5 August 2010
- ²⁰D. Kim, *Laminar flow past a sphere rotating in the transverse direction*, Journal of Mechanical Science and Technology **23** (2009) 578-589.
- ²¹T. A. Johnson and V. C. Patel, *Flow past a sphere up to a Reynolds number of 300*, J. Fluid Mech., **378** (1999) 19-70.
- ²²E. Achenbach, *Experiments on the Flow Past Spheres at Very High Reynolds Numbers*, J. Fluid Mech., **54**(3), (1972) pp. 565-575
- ²³G. S. Constantinescu and K. D. Squires, *LES and DES Investigations of Turbulent Flow over a Sphere*, AIAA Paper, AIAA-2000-0540